Propagation Characteristics of Exponential-Cosine Gaussian Vortex Beams

Xin Tong(童鑫) and Daomu Zhao(赵道木)*

Zhejiang Province Key Laboratory of Quantum Technology and Device, Department of Physics, Zhejiang University, Hangzhou 310027, China

We propose a controllable exponential-Cosine Gaussian vortex (ECGV) beam, which can evolve into the different beam profiles with three parameters: distance modulation factor (DMF), split modulation factor (SMF) and rotation modulation factor (RMF). When SMF is 0, the ECGV beam appears as a perfect single-ring vortex beam and the ring radius can be adjusted by the DMF. We deduce from mathematics and give the reason for the single-ring characteristics. When SMF is not 0, the beam splits symmetrically. DMF, SMF and RMF control the number, distance and rotation angle of the split, respectively. Our experiments verify the correctness of the theory.

Gaussian beams are well known and one of the most studied beam types in the study of optics. In 1971, Nye and Berry proposed the relationship between phase singularity and amplitude.[1] Coullet then proposed the concept of the optical vortex in 1989.[2] In 1992, Allen proposed that each photon in the beam containing $\exp(il\phi)$ carries the orbital angular momentum $l\hbar$, where l is called the topological charge (TC).[3] A large number of researchers have since conducted in-depth research and several derivative beams have been proposed, such as Hermite Gaussian beams, Laguerre Gaussian beams,[4−10] Bessel Gaussian beams,[11−15] and hollow sinh-Gaussian beams.[16−18] Meanwhile, in-depth research has been conducted on the phase of the beam and many new vortex beams with strange properties have been proposed, including asymmetric vortex beams,[19,20] fractional vortex beams,[21−24] spiral cone beams,[25,26] power-exponent phase vortex beams,[27−29] and vector beams.[30−32]

Generally, the manipulation and capture of particles can be achieved through beams.[33−36] However, traditional beams are limited when used to manipulate and capture particles because they cannot be controlled freely. This can create problems when controlling the captured particles accurately. The change of the TC of most traditional vortex beams is often accompanied by the change of their radii. This radius-TC interdependence will increase the complexity of the research.[37]

In this Letter, we propose a novel controllable ECGV beam. The arbitrary control of the beam can be achieved by changing the values of three parameters: DMF, SMF and RMF. DMF controls the distance of intensity profile, SMF controls the number of beam split, and RMF controls the rotation angle of the beam. In addition, we find that the beam will evolve into a bright single-ring vortex beam when SMF = 0. Its bright ring radius is affected by the value of DMF but is insensitive to low TCs, so it can be approximated as a perfect vortex beam.[38−43] If the radius of the beam does not change with the TCs, then the beam can be called a perfect vortex beam. This concept was first proposed by Ostrovsky and co-workers.[38] For SMF > 0, the ECGV beam will show interesting intensity profile characteristics. In particular, it splits in a petal-like shape to the surroundings. The number of splits is determined by the value of SMF, the splitting distance is affected by DMF, and the rotation angle of beam splitting is controlled by RMF.

Optical tweezers have been widely applied in the fields of physical, biomedical engineering and chemistry for particle capture and guidance. Besides the fundamental Gaussian beam, various beams with strange properties play a pivotal role in particle capture. However, the refractive index distribution of the particles and the environment is not stable, so the controllability of the beam becomes very important. The ECGV beam can generate different shapes by setting reasonable parameters, which greatly enhances the flexibility of control. The controllability feature of the ECGV beam may improve the efficiency of particle capture and guidance in the unstable refractive index medium. We have simulated and verified the characteristics of the ECGV beam in theory and experiment.

First, let us introduce the electric field expression of the ECGV beam as follows:

$$E_1(r,\phi) = \exp\left(-\frac{r^2}{\omega^2}\right)\exp\{\alpha r \cos[n(\phi+\zeta)]\}\exp(il\phi). \tag{1}$$

*Corresponding author. Email: zhaodaomu@yahoo.com

Here (r, ϕ) is the polar coordinates, ω is the beam waist of the Gaussian beam, l is an integer, known as the TC; α is the DMF, n is the SMF, ζ is the RMF. We will then discuss the intensity profile from two aspects: $n = 0$ and $n \neq 0$.

When $n = 0$, Eq. (1) can be simplified to

$$E_1(r, \phi) = \exp\left(-\frac{r^2}{\omega^2}\right)\exp(\alpha r)\exp(il\phi). \quad (2)$$

As is known, the complex amplitude distributions in the back (ρ, θ) and front planes (r, ϕ) of this system are related by the Collins formula[44]

$$\begin{aligned}&E_2(\rho, \theta, z)\\&= -\frac{ik}{2\pi B}\exp(ikz)\iint E_1(r, \phi)\exp\Big\{\frac{ik}{2B}\\&\quad \cdot [Ar^2 - 2r\rho\cos(\theta - \phi) + D\rho^2]\Big\}rdrd\phi,\end{aligned} \quad (3)$$

where (ρ, θ) is the polar coordinates of the output plane. A, B and D are the elements of the ray transfer matrix of the optical system, and z is the propagation distance. Substituting $E_1(r, \phi)$ from Eq. (2) into Eq. (3) yields

$$\begin{aligned}&E_2(\rho, \theta, z)\\&= -\frac{ik}{2\pi B}\exp(ikz)\iint \exp\Big(-\frac{r^2}{\omega^2}\Big)\exp(\alpha r)\exp(il\phi)\\&\quad \cdot \exp\Big\{\frac{ik}{2B}[Ar^2 - 2r\rho\cos(\theta - \phi) + D\rho^2]\Big\}rdrd\phi.\end{aligned} \quad (4)$$

Using the integral representation of the νth-order Bessel function of the first kind,

$$J_\nu(x) = \frac{i^{-\nu}}{2\pi}\int_{0}^{2\pi} \exp(i\nu\phi)\exp(ix\cos\phi)d\phi, \quad (5)$$

then combining Eqs. (4) and (5) yields

$$\begin{aligned}E_2(\rho, \theta, z) &= \frac{k}{B}i^{l-1}\exp\Big(ikz + \frac{ikD\rho^2}{2B}\Big)\exp(il\theta)\\&\quad \cdot \int_{0}^{\infty} \exp(-Mr^2)\exp(\alpha r)J_l\Big(\frac{k\rho r}{B}\Big)rdr,\end{aligned} \quad (6)$$

where $M = 1/\omega^2 - ikA/2B$, and $J_l(\cdots)$ represents the lth integer-order Bessel function of the first kind. We then use the Taylor series and the integral formula of the hypergeometric Kummer function to reach

$$\begin{aligned}&\int_{0}^{\infty} x^\mu\exp(-a^2x^2)J_\nu(gx)dx\\&= \Gamma\Big(\frac{\mu + \nu + 1}{2}\Big)\frac{g^\nu}{2^{\nu+1}a^{\mu+\nu+1}\Gamma(\nu + 1)}\\&\quad \cdot {}_1F_1\Big(\frac{\mu + \nu + 1}{2}, \nu + 1; \frac{-g^2}{4a^2}\Big).\end{aligned} \quad (7)$$

After putting Eq. (7) into Eq. (6) and taking the integrations, one obtains the final analytical expression of

the electric field at the output plane as

$$\begin{aligned}E_2(\rho, \theta, z) &= \frac{k}{B}i^{l-1}\exp\Big(ikz + \frac{ikD\rho^2}{2B}\Big)\exp(il\theta)\\&\quad \cdot \sum_{h=0}^{\infty}\frac{\alpha^h}{h!}\Big(\frac{k\rho}{B}\Big)^l\Gamma\Big(1 + \frac{h}{2} + \frac{l}{2}\Big)\\&\quad \cdot \frac{1}{2^{l+1}M^{1+\frac{h}{2}+\frac{l}{2}}\Gamma(l+1)}\\&\quad \cdot {}_1F_1\Big(1 + \frac{h}{2} + \frac{l}{2}, l + 1; \frac{-k^2\rho^2}{4MB^2}\Big),\end{aligned} \quad (8)$$

where ${}_1F_1(a, b; x)$ denotes the confluent hypergeometric function and $\Gamma(\cdots)$ is the Gamma function. The above equation represents the electric field expression of the ECGV beam with $n = 0$ through the paraxial optical system. We continue to study the distribution characteristics of intensity in free-space propagation. For a free space, the ray transfer matrix of distance z reads

$$\begin{pmatrix}A & B\\C & D\end{pmatrix} = \begin{pmatrix}1 & z\\0 & 1\end{pmatrix}. \quad (9)$$

Combining Eqs. (8) and (9) and using the first Kummer formula, we obtain the field distribution of the ECGV beam propagating in free space as follows:

$$\begin{aligned}&E_2(\rho, \theta, z)\\&= \Big(\frac{k}{B}\Big)^{l+1}i^{l-1}2^{-(l+1)}\exp(ikz)\exp\Big(\frac{ik\rho^2}{2z}\Big)\\&\quad \cdot \exp(il\theta)\sum_{h=0}^{\infty}|\text{HyGG}\rangle_{hl},\end{aligned} \quad (10)$$

$$\begin{aligned}|\text{HyGG}\rangle_{hl} &= \frac{\alpha^h}{h!}\rho^l M^{-(\frac{h+l+2}{2})}\frac{\Gamma(h/2 + l/2 + 1)}{\Gamma(l + 1)}\\&\quad \cdot {}_1F_1\Big(-\frac{h - l}{2}, l + 1; \frac{k^2\rho^2}{4Mz^2}\Big)\exp\Big(\frac{-k^2\rho^2}{4Mz^2}\Big),\end{aligned} \quad (11)$$

where h is the superposition coefficient. We know that $|\text{HyGG}\rangle_{hl}$ is the hth-order hypergeometric-Gaussian mode. Therefore, we can conclude from Eq. (10) that the ECGV beam can be regarded as the linear superposition of a series of HyGG modes.[45,46] By exploring the HyGG modes, we can better study the properties of the ECGV beam.

In the paraxial region ($\rho \to 0$), the value of the confluence hypergeometric function tends to 1. Because of the existence of ρ^l, the intensity of HyGG mode tends to 0. When ρ is large, the value of the confluence hypergeometric function tends to 0, so the intensity still tends to 0. Therefore, we can conclude that the intensity profile of the ECGV beam will show the characteristics of the doughnut shape with the continuous superposition of HyGG modes.

Figure 1 shows the radial intensity profile of HyGG modes with different superposition coefficients and TCs at the propagation distance $z = 0.1Z_R$. $Z_R = \pi\omega^2/\lambda$ is Rayleigh distance. It can be seen from the

figure that the radial intensity profile of all modes first increases and then decreases, and the peak intensity of the mode first increases and then decreases with the superposition coefficient h. That is to say, if h is large, then the intensity will be very small so that we can ignore their contribution.

Figure 1 also shows another interesting feature. The low TCs only affect low-intensity and low-order HyGG modes ($h = 0$, $h = 2$), which have little effect on the ECGV beam intensity profile. This shows that the ECGV beam has the properties of a perfect vortex beam. It is worth mentioning that, while there is no absolute perfect vortex beam, it can be achieved with the low TCs because the larger the TC, the stronger the effect of the vortex. Actually, if the intensity of the beam is distributed in a single ring, then it may have the characteristics of a perfect vortex. The larger the radius and the smaller the ring width, the more "perfect" the beam will be.
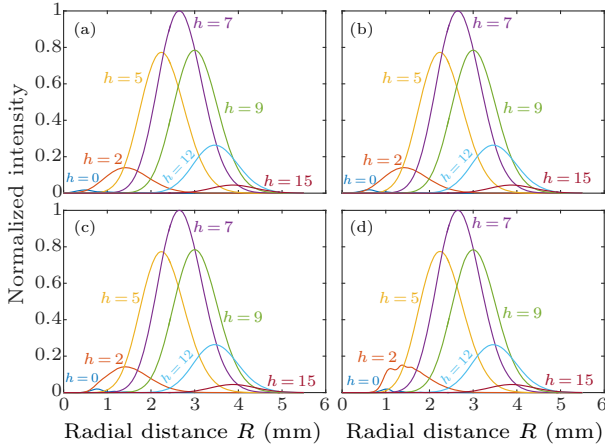

Fig. 1. The radial intensity profile of HyGG modes with different superposition coefficients and TCs: (a) $l = 1$, (b) $l = 2$, (c) $l = 4$, (d) $l = 8$. The parameters are $\omega = 2\,\text{mm}$, $\alpha = 2\,\text{mm}^{-1}$ and $z = 0.1Z_R$.

As mentioned in the above discussion, if ρ tends to 0, the value of $|\text{HyGG}\rangle_{hl}$ tends to 0 due to the action of ρ^l. However, if the TC is 0, $\rho^l \neq 0$, the intensity of HyGG is no longer zero and will be affected by other factors. The $|\text{HyGG}\rangle_{hl}$ reduces to the $|\text{HyGG}\rangle_{h0}$ and putting it into Eq. (11), we can find that only the coefficient h and the propagation distance z affect HyGG modes. Consequently, we discuss the influence of z and h on HyGG modes. Take some appropriate superposition coefficients at different propagation distances to calculate the normalized intensity of HyGG modes and ECGV beam. The results are shown in Fig. 2.

It is worth noting that if and only if $h = l = 0$, HyGG mode will reduce to the typical Gaussian mode but its intensity is very small compared to other modes, so this special case can be ignored, and its field distribution is still a dark hollow bright ring. We only take $h = 0$–15. Because when h is relatively large, there are factors $1/h!$ and $M^{-(h/2+l/2+1)}$ in the summation symbol, the sum term $|\text{HyGG}\rangle_{h0} \to 0$, whose

impacts on the ECGV beam are almost negligible. Therefore, only low-order HyGG modes play an important role in the ECGV beam. From Figs. 2(b)–2(e), we can conclude that when the propagation distance is relatively short, the normalized intensity of HyGG modes with different summation coefficients is very low at the paraxial position. However, as the propagation distance increases, the intensity of the HyGG modes corresponding to each h value increases at the central position. That is to say, the ECGV beam presents a single-ring characteristic when it propagates at a short distance. However, as the propagation distance increases, the single-ring characteristic gradually disappears. Instead, the intensity at the paraxial position continues to increase, appearing as a central bright spot. The intensity profile of the ECGV beam at different propagation distances is shown in Fig. 2(a) and its phase comes only from propagation in free space $\exp(ikz)$.
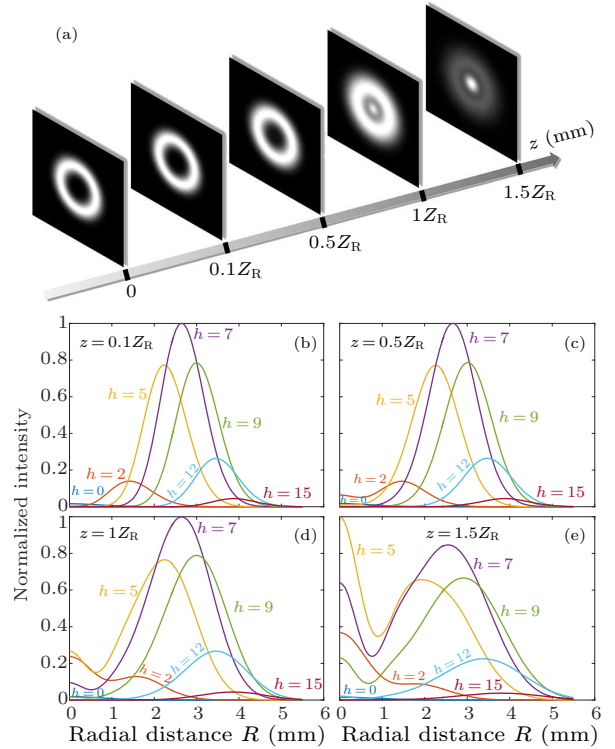

Fig. 2. Normalized intensity of the ECGV beam and HyGG modes at different propagation distances. (a) Normalized intensity of the ECGV beam. (b)–(e) Normalized intensity of HyGG modes with superposition coefficient $h = 0$–15. The parameters are $\lambda = 532.8\,\text{nm}$, $\omega = 2\,\text{mm}$, $\alpha = 2\,\text{mm}^{-1}$ and $l = 0$.

Combining Eq. (10) and Fig. 2, we can conclude that the ECGV beam is superimposed by different HyGG modes. These modes have different evolution forms during the propagation process, so they interact and interfere during long-distance propagation, thus forming the character of the central bright spot.

The expression of the ECGV beam is shown in Eq. (1). Let $\psi = \phi + \zeta$, then Eq. (1) can be expressed

as

$$E_1(r, \phi) = \exp\left(-\frac{r^2}{\omega^2}\right)\exp[\alpha r \cos(n\psi)]\exp(il\psi)$$
$$\cdot \exp(-il\zeta). \tag{12}$$

Comparing Eqs. (12) with (1), we can see that the function of RMF is actually to perform a rotational transformation of the cylindrical coordinates. In other words, the intensity will rotate with the change of ζ, which is a very interesting property. For ease of calculation, we set ζ to 0. Equation (1) performs amplitude modulation on the Gaussian beam. According to the physical properties, we can define amplitude modulation as a transmittance function

$$T(r, \phi) = \exp[\alpha r \cos(n\phi)]. \tag{13}$$

Obviously it is a periodic function. For $n = 1$, through coordinate transformation, we can obtain $\alpha r \cos(n\phi) = \alpha x$. Therefore, Eq. (1) can be expressed

as

$$E_1(x, y) = \exp\left(-\frac{(x - \beta)^2 + y^2}{\omega^2}\right)\exp(\beta^2)$$
$$\cdot \exp\left[il\tan^{-1}\left(\frac{y}{x}\right)\right], \tag{14}$$

where $\beta = \alpha\omega^2/2$. We can conclude from Eq. (14) that the ECGV beam is a Gaussian vortex-like beam. For $n = 1$, the ECGV beam will move along the x-axis, and the distance β is controlled by the DMF. Due to the existence of the cosine term, Eq. (13) is a periodic function, so the transmittance function will traverse n cycles in the range of 0–2π. Combining the result of $n = 1$, we know that the ECGV beam will move along the radial direction after one cycle, with the argument of $2\pi/n$, and the moving distance is also β. In summary, the number of lobes of ECGV beam splitting is the same as the number of cycles, which is the value of SMF.
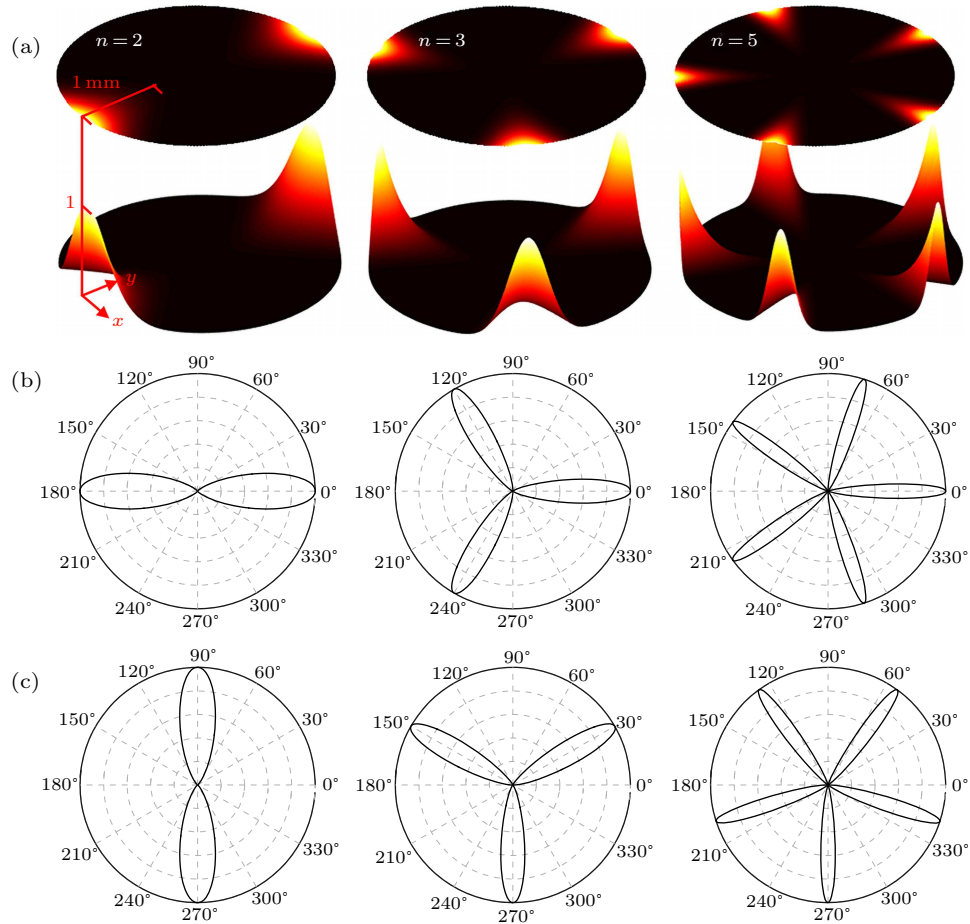

Fig. 3. The first, second and third columns, respectively, represent the transmittance distribution at $n = 2$, $n = 3$ and $n = 5$. Row (a), $\zeta = 0°$. Row (b) $r = 2$, $\zeta = 0°$. Row (c), $r = 2$, $\zeta = 90°$. The parameter is $\alpha = 2\,\mathrm{mm}^{-1}$.

To describe this characteristic more intuitively, we have carried out a numerical simulation. Figure 3 shows the transmittance distribution at different SMFs and the situation when only RMF is changed in polar coordinates. It can be seen from the figure that

the transmittance function has a great dependence on SMF, and the number of peaks and the number of lobes in polar coordinates are the same as the value of SMF. If RMF changes $\Delta\zeta$, then the "petal diagram" in polar coordinates will also rotate $\Delta\zeta$ clock-

wise accordingly. This is consistent with the above analysis. From the above analysis, we can easily infer that the intensity profile of the ECGV beam on the observation surface has a periodic rotation and shows the characteristic of the symmetrical splitting, and its split number should be the same as the value of SMF at $n \neq 0$. When propagating in free space, the Fourier optical transmission method can be used to calculate the electric field distribution at the output plane.
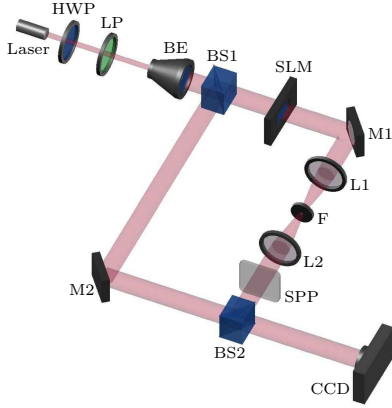

Fig. 4. Experimental setup for generating an ECGV beam: HWP, half-wave plate; LP, linear polarizer; BE, beam expander; BS1, BS2, beam splitters; SLM, spatial light modulator; M1, M2, mirror reflector; L1, L2, lenses; F, filter; SPP, spiral phase plate; CCD, charge-coupled device.

We next generate the ECGV beam with $n = 0$ and $n \neq 0$ in the experiment at propagation distance z in free space. The spatial light modulator (SLM, LC2012) can modulate the beam, so we use it to generate the ECGV beam and explore its intensity profile and characteristics on the output plane. A Mach–Zehnder interferometry is used to study the vortex characteristics of the beam. The experimental device used to generate the ECGV beam is shown in Fig. 4. The beam is produced by a 532.8 nm linearly polarization He–Ne laser. A half-wave plate (HWP) and a linear polarizer (LP) are placed behind the He–Ne laser. The HWP can be used to adjust the polarization direction of the beam. The LP can adjust the polarization direction of the beam to be consistent with the polarization working direction of the SLM. Consequently, they can be used to control the power of the incident beam. After the beam expander (BE), the spot radius is adjusted to 2 mm. The beam splitter, BS1, separates the conditioned beam onto a reference beam and an object beam. The object beam first achieves amplitude modulation through SLM, and then passes through the $4f$ system after being reflected by the mirror M1, the purpose is to select the required modulated beam. The focal lengths of the lenses L1 and L2 are both 100 mm. The modulated beam through the spiral phase plate (SPP) to produce an ECGV beam. The reference beam is reflected by the mirror M2. BS2 joins the reference beam and the object beam. If we

block the reference beam, the intensity distribution of the beam is formed on the observation plane. On the contrary, the reference beam and the object beam interfere with each other to form an interference pattern. We next generate the ECGV beam with $n = 0$ and $n \neq 0$ in the experiment at propagation distance z in free space.

The intensity is shown in Fig. 5 for different values of TC. For comparing and verifying the experimental results, the calculation results of Eq. (10) are shown in the same figure. The ring radius of the ECGV beam is independent of the low TCs. When the DMF is constant, the ring radius almost remains unchanged with the increase of the TC. This matches the characteristics of the perfect vortex beam.
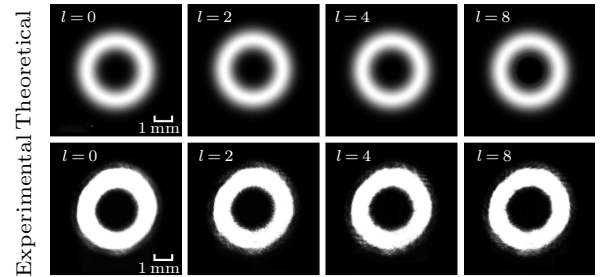

Fig. 5. Theoretical and experimental results of the ECGV beam with $\alpha = 2\,\text{mm}^{-1}$ at the propagation distance $z = 1800\,\text{mm}$ for different values of TC. The parameters are $\lambda = 532.8\,\text{nm}$, $\omega = 2\,\text{mm}$ and $n = 0$.
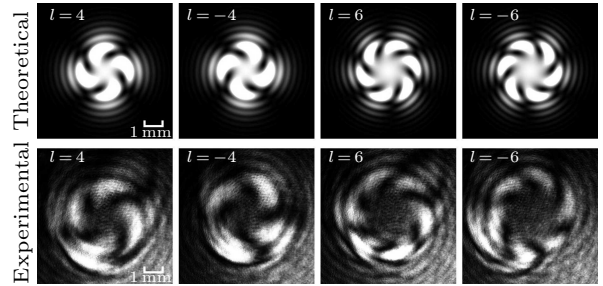

Fig. 6. Theoretical and experimental results of the interference pattern for different values of TC.

We verify its vortex properties by interferometry. Figure 6 shows the interference pattern obtained by the interference between the object beam and the reference beam. We can find that the pattern takes the shape of a "spiral petal", which confirms the existence of OAM in the perfect vortex beam. The number of petals is equal to the number of TCs, and the sign of the TC determines the direction of rotation. The size of the ring radius is affected by α and the relationship between α and the radius of the ring is shown in Fig. 7. According to Eq. (2), it degenerates into a traditional vortex beam for $\alpha = 0$. We can conclude that the radius of the ring is affected by DMF.

From Figs. 5 and 7(b)–7(e), it can be seen that under the condition that the TC remains unchanged, as α gradually increases, the dark ring disappears until a single bright ring is formed. Therefore, we judge that

there is a vortex core in the dark hollow area, and the radius is affected by the TC. The larger the TC, the larger the radius of the vortex core, so the larger the influence of vortices. In other words, the larger the DMF, the smaller the influence brought by the TC. Figure 8 shows the intensity profile with different l. It can be seen that when the TC is small, the intensity profile still presents single ring characteristics. However, when the TC is very large, many light and dark rings appear in the original single bright ring, which shows that the ring is affected by the vortex.
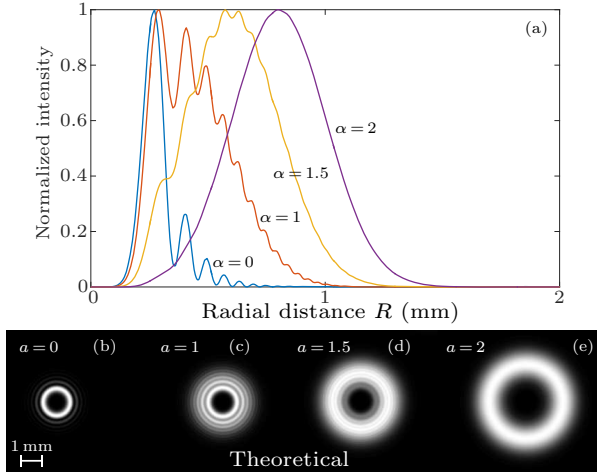

Fig. 7. The relationship between α and ECGV beam. (a) Normalized radial intensity profiles of the ECGV beam with different α. (b)–(e) The intensity profile of the output plane with different α (mm^{-1}). The parameters are $\lambda = 532.8$ nm, $\omega = 2$ mm, $z = 1800$ mm and $l = 4$.

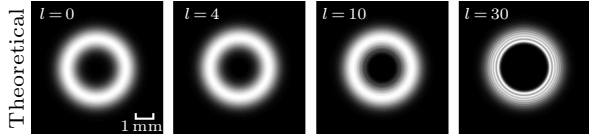**Fig. 8.** Numerical results of intensity profile with different TCs. The parameters are $\lambda = 532.8$ nm, $\omega = 2$ mm, $\alpha = 2$ mm^{-1} and $z = 1800$ mm.

When $n \neq 0$, the analysis shows that the ECGV beam will split symmetrically around and will be affected by DMF, SMF and RMF. Figure 9 shows the intensity profile at different SMFs and RMFs. It can be clearly seen from the figure that the number of splits of the ECGV beam is the same as the value of SMF, and the rotation angle is the same as the value of RMF.

In the case of $n = 0$, the value of DMF is associated with the radius of the bright ring. In the same way, we can speculate that the effect of DMF should be related to the split distance. Figure 10 takes $n = 3$ as an example to show the intensity profile with different DMFs. It can be seen from the figure that the greater the α, the greater the distance between the symmetrical splitting of each lobe. Therefore, theoretically, we can achieve arbitrary control of the beam

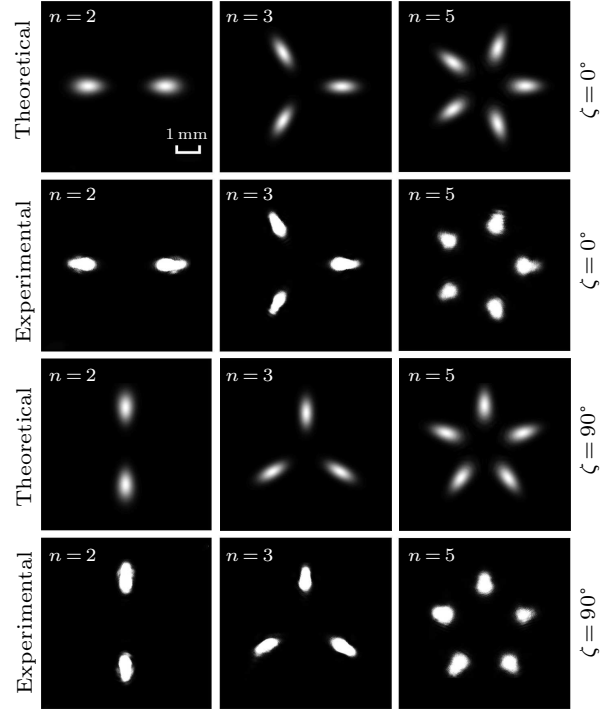by adjusting the values of DMF, SMF and RMF.

Fig. 9. Theoretical and experimental results of the ECGV beam with $\alpha = 2$ mm^{-1} at the propagation distance $z = 1800$ mm for different values of SMF and RMF. The parameters are $\lambda = 532.8$ nm, $\omega = 2$ mm and $l = 0$.
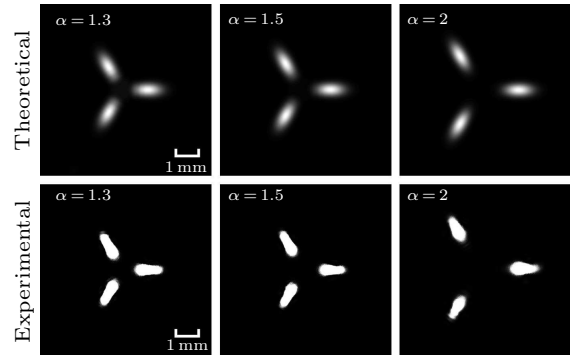

Fig. 10. Theoretical and experimental results of intensity profile with different α at the propagation distance $z = 1800$ mm. The parameters are $\lambda = 532.8$ nm, $\omega = 2$ mm, $l = 0$ and $n = 3$.

In summary, we have proposed a novel controllable ECGV beam, which is controlled by three parameters: DMF, SMF and RMF. For SMF $n = 0$, the ECGV beam presents a bright single-ring intensity profile and the size of the bright ring radius can be controlled by the value of DMF. Starting from the Collins formula, we find through mathematical derivation that the ECGV beam is superimposed by different HyGG modes, thus forming a single ring characteristic. When the ECGV beam does not contain the vortex (TC = 0) and the propagation distance is large, the single-ring characteristic of the beam disappears and intensity appears in the dark hollow area. In addition, it is not sensitive to low TCs, so it conforms to the

characteristics of the perfect vortex beam. However, when the TC increases, the influence of the vortex on the beam becomes more and more obvious.

For SMF $n \neq 0$, the amplitude modulation term in the ECGV beam is periodic, so the beam will split symmetrically around, and DMF, SMF, RMF control the number, distance and rotation angle of the beam split, respectively. However, the mathematical expression of $n \neq 0$ is not given here, and only the propagation characteristics in free space are discussed. Therefore, in our future work, we will continue to conduct extended research on it, hoping to get more general results.

Finally, the designed experiment verifies the properties of the ECGV beam. Therefore, we can control the beam arbitrarily through these parameters, which reflects a high degree of maneuverability. This is conducive to the precise capture and guidance of particles.

References

[1] Nye J F and Berry M V 1971 *Proc. R. Soc. A* **336** 165
[2] Coullet P, Gil L and Rocca F 1989 *Opt. Commun.* **73** 403
[3] Allen L, Beijersbergen M, Spreeuw R and Woerdman J 1992 *Phys. Rev. A* **45** 8185
[4] Allen L and Padgett M J 2000 *Opt. Commun.* **184** 67
[5] Beijersbergen M W, Allen L and Woerdman J P 1993 *Opt. Commun.* **96** 123
[6] Turnbull G A, Robertson D A, Smith G M, Allen L and Padgett M J 1996 *Opt. Commun.* **127** 4
[7] Zhou G, Wang F, Chen R and Li X 2020 *Opt. Express* **28** 28518
[8] Fan X, Ji X, Wang H, Deng Y and Zhang H 2021 *J. Opt. Soc. Am. A* **38** 168
[9] Zhou G, Wang F and Feng S 2020 *Opt. Express* **28** 19683
[10] Ge Z, Zhou Z, Li Y, Yang C, Liu S and Shi B 2021 *Opt. Lett.* **46** 158
[11] Seshadri S R 2002 *Opt. Lett.* **27** 998
[12] April A 2011 *J. Opt. Soc. Am. A* **28** 2100
[13] Bagini V 1996 *J. Mod. Opt.* **43** 1155
[14] Jordan R H and Hall D G 1994 *Opt. Lett.* **19** 427
[15] Greene P L and Hall D G 1996 *J. Opt. Soc. Am. A* **13** 962
[16] Kuga T, Torii Y, Shiokawa N, Hirano T, Shimizu Y and Sasada H 1997 *Phys. Rev. Lett.* **78** 4713
[17] Yan M, Yin J and Zhu Y 2000 *J. Opt. Soc. Am. B* **17** 1817
[18] Mei Z and Zhao D 2005 *J. Opt. Soc. Am. A* **22** 1898
[19] Terriza G M, Wright E M and Torner L 2001 *Opt. Lett.* **26** 163
[20] Alexander T J, Sukhorukov A A and Kivshar Y S 2004 *Phys. Rev. Lett.* **93** 63901
[21] Basistiy I V, Pasko V A, Slyusar V V, Soskin M S and Vasnetsov M V 2004 *J. Opt. A* **6** 166
[22] Götte J B, Holleran K O, Preece D, Flossmann F and Padgett M J 2008 *Opt. Express* **16** 993
[23] Wen J, Wang L, Yang X, Zhang J and Zhu S 2019 *Opt. Express* **27** 5893
[24] Hosseini S M, Akhlaghi E A and Saber A 2020 *Opt. Lett.* **45** 3478
[25] Alonzo C A, Rodrigo P J and Glückstad J 2005 *Opt. Express* **13** 1749
[26] Hermosa N, Guzmán C R and Torres J P 2013 *Opt. Lett.* **38** 383
[27] Li P, Liu S, Peng T, Xie G and Zhao J 2014 *Opt. Express* **22** 7598
[28] Lao G, Zhang Z and Zhao D 2016 *Opt. Express* **24** 18082
[29] Shen D, Wang K and Zhao D 2019 *Opt. Express* **27** 24642
[30] Zhong J, Qi S, Liu S, Li P and Zhao J 2019 *Opt. Lett.* **44** 3849
[31] Zhang Y, Li P, Liu S and Zhao J 2016 *Opt. Express* **24** 28409
[32] Guo X, Li P, Zhong J and Zhao J 2020 *Laser & Photon. Rev.* **14** 1900366
[33] Grier D G 2003 *Nature* **424** 810
[34] Simpson N B, Dholakia K, Allen L and Padgett M J 1997 *Opt. Lett.* **22** 52
[35] Prentice P, Macdonald M, Frank T, Cuschieri A and Dholakia K 2004 *Opt. Express* **12** 593
[36] Yao A and Padgett M J 2011 *Adv. Opt. Photon.* **3** 161
[37] Simpson S H and Hanna S 2010 *J. Opt. Soc. Am. A* **27** 1255
[38] Ostrovsky A S, Rickenstorff P C and Arrizón V 2013 *Opt. Lett.* **38** 534
[39] Vaity P and Rusch L 2015 *Opt. Lett.* **40** 597
[40] García J, Rickenstorff P C, Ramos G R, Arrizón V and Ostrovsky A S 2014 *Opt. Lett.* **39** 5305
[41] Chen M, Mazilu M, Arita Y, Wright E M and Dholakia K 2013 *Opt. Lett.* **38** 4919
[42] Pinnell J, Rodríguez F V and Forbes A 2019 *Opt. Lett.* **44** 5614
[43] Li P, Zhang Y, Liu S and Zhao J 2016 *Opt. Lett.* **41** 2205
[44] Collinst S A 1970 *J. Opt. Soc. Am.* **60** 1168
[45] Sun Q, Zhou K, Fang G, Zhang G, Liu Z and Liu S 2012 *Opt. Express* **20** 9682
[46] Karimi E, Zito G, Piccirillo B, Marrucci L and Santamato E 2007 *Opt. Lett.* **32** 3053